THE EUROPEAN
PHYSICAL JOURNAL PLUS

Vibration prediction and failure analysis based on refined modeling of turbocharging rotor system with variable cross sections

Longkai Wang[1,2,a]**, Ailun Wang**[1,2,b] (iD)**, Miao Jin**[2]**, Yijun Yin**[1]

[1] Light Alloy Research Institute, Central South University, Changsha 410083, China
[2] State Key Laboratory of High Performance Complex Manufacturing, Central South University, Changsha 410083, China

Abstract This paper proposes a general refined modeling method to establish the mathematical model of the turbocharger flexible rotor system for exact dynamics prediction and failure analysis. Based on the FE method and Guyan matrix reduction, the mathematical model of the rotor with multiple variable cross sections is developed. Then, the motion governing equation of the rotor-bearing system is derived by combining the refined rotor model with the floating ring equation. In order to verify the modeling method, a series of comparisons of simulations and tests are introduced. In addition, the reasons for the enlargement of compressor end bearing inner clearance are revealed. After that, the influence of the bearing inner clearance on the vibration characteristics is discussed, while the rotor with and without unbalance defect is considered. The results show that the variation of the bearing inner clearance will not only affect the stability, but also the overall amplitude as well as 3D processional orbits. The usage of the proposed rotor modeling method is more time efficient compared to the common modeling methods and is capable to effectively perform parametric studies. The research is helpful to predict dynamic behaviors of complex rotors more accurately and prevent from failure.

1 Introduction

Exhaust gas turbocharging technology is an important way to cut fuel consumption and improve engine power performance. This technology has been widely employed in diesel and gasoline engines. For example, few diesel engines today do not have turbochargers. Furthermore, a wide variety of gasoline engines available on the market are equipped with one or two turbochargers.

The small size automotive turbocharger, as a typical high-speed turbomachinery, can operate above 200,000 r/min due to the good damping effect of the bearing, which is much higher than other rotary machineries. Commonly, automotive turbocharger rotors are mounted on the floating ring bearing composed of a freely rotating floating ring with a speed smaller

a e-mail: Longkai.Heat@hotmail.com (corresponding author)

b e-mail: walcsu@163.com (corresponding author)

Springer

than the journal one. The design of two oil-films linked in series by a floating ring can provide better damping effects as well as fewer friction losses than single-film plain journal bearings. However, the inner oil-film and outer oil-film can become unstable due to its high nonlinearity in nature and the high-speed operating conditions for turbochargers. Thus, floating ring bearings can induce a variety of self-excited vibrations (resulted from the inner/outer oil-film instability) in a wide speed region. Surprisingly, the high nonlinearity of floating ring bearings is capable of generating controlled limit cycles in these unstable regions, which can still ensure the safe operation of turbochargers under normal design conditions [1–3]. As everyone knows, dynamic characteristics of the turbocharger rotor supported in nonlinear floating ring bearings is very sensitive to the rotor-bearing parameters. In some cases, the turbocharger can become total unstable due to the wrong design of the rotor and the bearing, which results in fatal failure [1, 4–9]. Therefore, building a refined model of the turbocharger flexible rotor with multiple variable cross sections in the axial direction is of great importance to predict the complex dynamic behaviors of turbochargers, and to prevent rotor from failure caused by bearing degradation in advance.

As turbochargers are generally used in passenger car applications, how to establish a more refined model of turbocharger flexible rotor system with multiple variable cross sections by mathematical formulation and predict the dynamical behaviors more accurately are the heart of the matter. Driven by the design goals of high-efficiency and low-amplitude turbochargers, the nonlinear dynamics and stability of turbochargers have always been the focus of attention of many scholars. By using correlation coefficient method and global sensitivity method, Koutsovasilis et al. [10] quantitatively studied the sub-synchronous vibration of turbocharger rotors. Based upon additive manufacturing techniques, Andrearczyk et al. [11] creatively studied the vibration characteristics of a turbocharger with a plastic compressor impeller. Thrust bearings are also an important part of the turbocharger, the computational model and the structure design were discussed by Novotný et al. [12–15]. By using the linear and nonlinear Campbell diagrams, Woschke et al. [16] focused on the excitation mechanisms of turbocharger rotors with floating ring bearings. In order to suppress sub-synchronous vibrations, some new designs about lubrication grooves were discussed by Smolík et al. [17]. In view of sub-synchronous vibrations generated by fluid-film instability, Kirk et al. [18] presented a method for improving the rotor stability by introducing unbalance. In addition, the instability phenomenon of turbocharger rotors was observed by the vibration experiment on an automotive engine [19]. After that, they proposed a novel design concept of radial tilting pad bearing to suppress the sub-synchronous motion amplitude [20]. Dyk et al. [21] studied the effects of various analytical model of floating ring bearings, in which a general model was provided by correction polynomials. By simplifying the two oil-film bearing into a single-film bearing, Ying et al. [22] studied the vibration of a turbocharger rotor with engine excitation. Li [23] presented a finite length bearing model for the prediction of the stability. Using the multi-body dynamic modeling method, Schweizer [5] discussed total instability phenomena. Feng et al. [24] presented some suggestions for the outer clearance of semi-floating ring bearings. Considering the manufacturing errors of the floating ring, Wang et al. [25] proposed a relatively well inner and outer clearance combination, and then investigated the unbalance location effect on the nonlinear vibration characteristics of a small turbocharger [26]. After that, BIN et al. [27, 28] proposed some qualitative reference data for floating ring bearing design in axial length and inlet oil temperature. Tian et al. [3, 29] discussed the floating ring bearing outer clearance effects on the rotor stability. The result shows that the wrong design can result in total failure at high speeds. The inner-outer clearance ratio effect on the sub-synchronous vibration components was investigated by Smolík et al. [30]. The presented data shows that some clearance ratio can greatly reduce the magnitude of the sub-synchronous

vibration. There are two major failure modes for turbochargers. One is compressor impeller damage (degradation of the compressor vanes [8, 9]), the other is shaft fracture failure at turbine hub. Surprisingly, observations of various failed turbochargers have shown that the compressor end bearing was damaged more than the turbine end bearing. Namely, the inner surface of the floating ring in the compressor end bearing was worn over time, continuing to increase the inner clearance until turbocharger failure. Thus, further study of the vibration prediction and failure analysis is the key to the dynamical design of high-speed turbochargers, as well as to prevent from failures during operation in advance.

The research stated above shows that the stability, sub-synchronous vibrations, bifurcation and motion orbits of turbocharger rotors with floating ring bearings are closely related to the rotor-bearing structure. Although a lot of research has been done on the stability of turbochargers, the effects of the bearing inner clearance on nonlinear dynamics as well as stability have not been studied in-depth, and there are needs to conduct failure analysis. In the published literatures, there is no report on the refined modeling of turbocharger rotors. In most cases, the rotor is simplified into a four-nodes-three-elements model without fully considering the variable cross-section rotor feature.

In order to accurately predict the dynamics behavior during operation and the failure, this work proposes a general refined mathematical model of turbocharger rotor based on FE method and Guyan reduction. By coupling the nonlinear oil-film forces of floating ring bearings with the motion equation of rotor-ring system, a 11-master-nodes (10 master element) coupling total 41 sub-elements rotor-bearing dynamic model is developed. Newmark-beta numerical method is adopted to solve the governing equations of motion. The mode shape, potential energy distribution, frequency spectrum, 3D processional orbit and amplitude-frequency response curve are used to show the dynamic behaviors of turbocharger rotor in floating ring bearings. Besides, the effect of some key parameters, including the bearing clearance and unbalance, is also discussed. Moreover, the failure is also examined.

This paper is organized as follows. Section 2 derived the refined governing equation of motion of the turbocharger rotor-floating ring system, in which the bearing model, rotor model and rotor-floating ring model were developed. Secondly, the failure was first revealed from the linear point of view and the test data, and the established model is validated in Sect. 3. Next, parametric investigation about inner clearance with and without unbalance defect and dynamic behavior prediction were performed in Sect. 4, in which the failure was further explained. Finally, some conclusions are drawn in Sect. 5.

Based on previous researches, it can be seen that the non-uniform cross-section feature of the rotor is often neglect in the past, and turbocharger rub-impact failure was not studied in-depth and quantitative replacement advice was also not given. This work innovatively proposes a refined rotor dynamic modeling method which considers the variable section characteristics of rotor, based on FE method and Guyan DOF reduction theory. For the support mechanics model, full consideration is given to the flexibility of the support foundation, the characteristics of the double-layer oil-film, and the temperature difference between the inner and outer oil-films. Novelty, the causes of rub between the compressor impeller and volute of turbochargers and the failure mechanism for the whole machine are revealed, and some quantitative suggestions for bearing replacement are also put forward. This work can provide new insight to the turbocharger designers and maintainer and the results in this paper can be used to present turbochargers from failure caused by bearing wear and become the basis for redesigning bearings. What's more, the proposed rotor modeling method has a wide range of application value.

2 Motion equation of turbocharging rotor in floating ring bearings

Turbochargers are widely equipped in diesel engines and gasoline engines. Different from the application in diesel engines, automotive turbochargers run in a wide speed region and are small in size. To establish a refined model for predicting the dynamic behaviors of high-speed turbocharger rotors with floating ring bearings, a practical turbocharger (see Fig. 1) employed in gasoline cars is taken as the research object, which is composed of a compressor and a turbine embedded in a single shaft, as shown in Figs. 1a and 2a.

Floating ring bearings (see Fig. 2b) are the most common hydrodynamic bearing type used for small automotive turbochargers. The strong nonlinearity of two oil-films and the high-speed operating condition will cause the turbocharger exhibit a variety of vibration problems. Two supported bearings are identical in design and share the lubrication system. The internal clearance of the bearing is kept very tight to control the rotor movement, generally, < 1 mil (~ 0.02 mm) while the external clearance is > 3 mils (~ 0.08 mm) [31]. Figure 3a–e shows the variation of inner clearance on the compressor end bearing.

In order to establish the dynamic model and to predict the dynamics behaviors, in terms of the complicated structure feature and high nonlinearities, the mathematical model of the rotor-bearing system is established based on the following assumptions:

1. Impellers are equivalent into a series of massless conical elements [32, 33] and cylindrical elements. Associated mass, rotational moment inertia and center of gravity position are obtained by using the three-dimensional CAE software, then, applying it to the total motion governing equations in the form of rigid disk motion equation.
2. Small torsional and axial vibrations are both ignored.
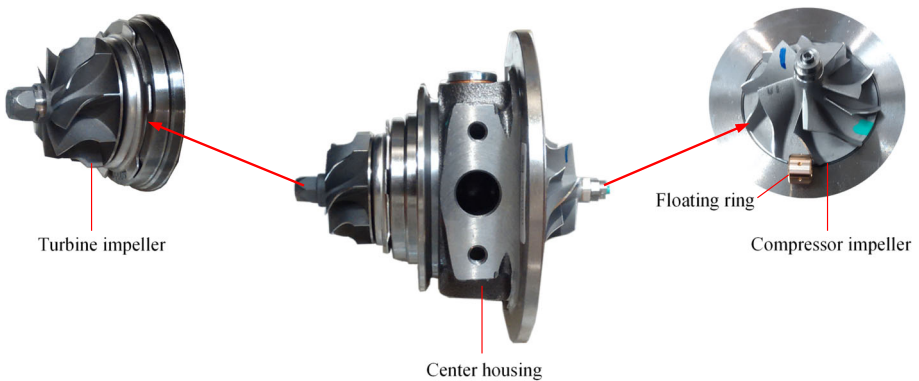3. Small chamfers and rounded corners are omitted.
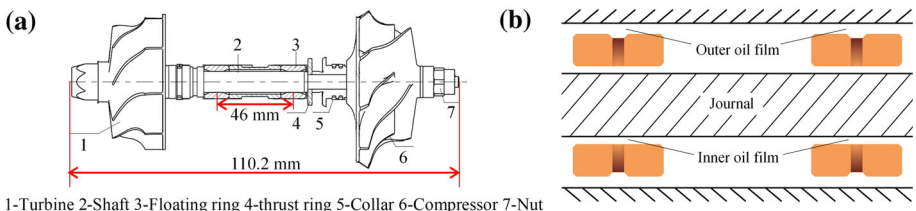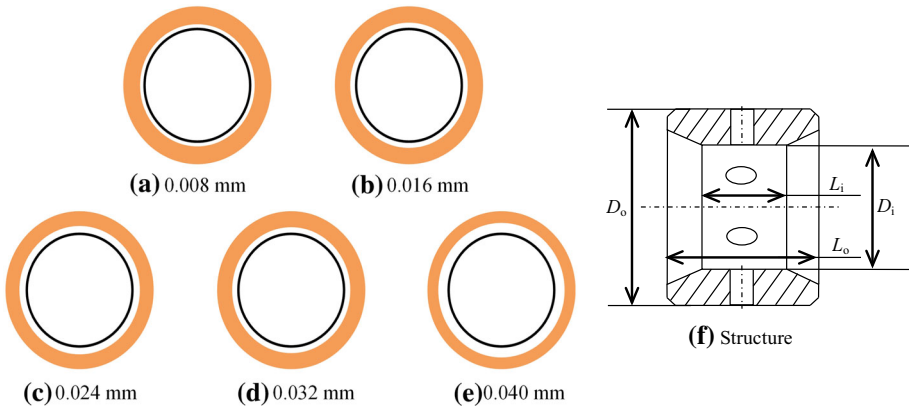

Fig. 1 Automotive turbocharger

1-Turbine 2-Shaft 3-Floating ring 4-thrust ring 5-Collar 6-Compressor 7-Nut

Fig. 2 Turbocharger rotor assembly (**a**) and floating ring bearings (**b**)

(a) 0.008 mm   **(b)** 0.016 mm

(c) 0.024 mm   **(d)** 0.032 mm   **(e)** 0.040 mm

(f) Structure

Fig. 3 Compressor end bearing inner clearance variation due to operation wear over time

4. Floating rings are considered as rigid bodies.
5. Six oil supply holes of each ring are neglected.
6. The lubricating flow oil-film is considered to be an isothermal, incompressible laminar flow.

2.1 Mathematical model of floating ring bearing

A general floating ring bearing can be treated as two oil-films in series (see Fig. 2b) through a rigid floating ring with an angular speed of Ω_i. The inner flow oil-film links the journal to the floating ring, and the outer flow oil-film links the rigid floating ring to the bearing shell. The inner hydrodynamic bearing possesses, in particular, two rotating surfaces, i.e., journal outside surface and floating ring inner surface, while the outer hydrodynamic bearing has only one rotation surface. Based upon the Navier–Stokes's equations and continuity equations, the general Reynolds equations for solving the pressure distributions in both inner and outer oil-films are deduced as follows:

$$\frac{1}{R_j^2} \frac{\partial}{\partial \theta_i} \left(\frac{h_i^3}{12\mu_i} \frac{\partial p_i}{\partial \theta_i} \right) + \frac{\partial}{\partial z_i} \left(\frac{h_i^3}{12\mu_i} \frac{\partial p_i}{\partial z_i} \right) = \frac{\Omega_i}{2} \frac{\partial h_i}{\partial \theta_i} + \frac{\partial h_i}{\partial t}, \tag{1}$$

$$\frac{1}{R_{ro}^2} \frac{\partial}{\partial \theta_o} \left(\frac{h_o^3}{12\mu_o} \frac{\partial p_o}{\partial \theta_o} \right) + \frac{\partial}{\partial z_o} \left(\frac{h_o^3}{12\mu_o} \frac{\partial p_o}{\partial z_o} \right) = \frac{\Omega_r}{2} \frac{\partial h_o}{\partial \theta_o} + \frac{\partial h_o}{\partial t}, \tag{2}$$

$$\Omega_i = \Omega_j + \Omega_r, \tag{3}$$

$$h_i = C_i - x_{jr} \cos \theta_i - y_{jr} \sin \theta_i, \tag{4}$$

$$h_o = C_o - x_r \cos \theta_o - y_r \sin \theta_o, \tag{5}$$

$$\frac{\partial h_i}{\partial t} = -(\dot{x}_{jr} \cos \theta_i + \dot{y}_{jr} \sin \theta_i), \tag{6}$$

$$\frac{\partial h_o}{\partial t} = -(\dot{x}_r \cos \theta_o + \dot{y}_r \sin \theta_o), \tag{7}$$

where subscripts i, o, j and r distinguish parameters of the inner film, the outer film, the journal and the floating ring, respectively; R_j and R_{ro} represent, respectively, the journal radius and the ring outer radius; θ and z are, respectively, the angular coordinate originated

Fig. 4 Middle plane of a floating ring bearing
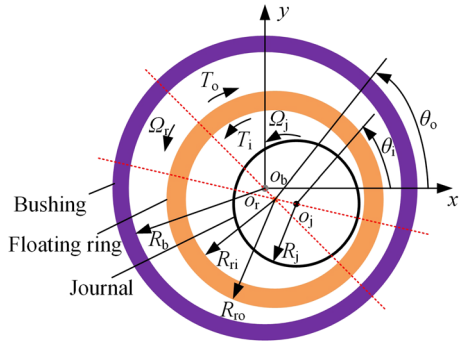
from the x direction and the axial coordinate (see Fig. 4); h is the film thickness; μ is the viscosity. p represents the oil pressure distribution; Ω is the angular speed in rad/s; t is the time parameter; C indicates the bearing radius clearance; x_{jr} and y_{jr} denote, respectively, the relative displacements between the journal and the ring in the x and y directions; x_j and y_j, x_r and y_r are, respectively, the displacements of the journal and the ring. The rotational speed of the ring can be determined by the balance of friction torques from the inner and outer oil-films [34]. The friction torque on the ring from the inner oil-film is

$$T_i = \iint R_j^2 \tau_i \, d\theta_i \, dz_i, \tag{8}$$

where

$$\tau_i = \frac{\mu_i R_j (\Omega_j - \Omega_r)}{h_i} - \frac{h_i}{2R_j} \frac{\partial p_i}{\partial \theta_i}. \tag{9}$$

The friction torque on the ring from the outer oil-film is

$$T_o = \iint R_{ro}^2 \tau_o \, d\theta_o \, dz_o, \tag{10}$$

where

$$\tau_o = \frac{\mu_o R_{ro} \Omega_r}{h_o} - \frac{h_o}{2R_{ro}} \frac{\partial p_o}{\partial \theta_o}. \tag{11}$$

When eccentricity ratios approach zero, the ring-journal speed ratio can be defined as

$$v = \frac{\Omega_r}{\Omega_j} = \frac{1}{1 + \left[\left(\frac{\mu_o}{\mu_i} \right) \left(\frac{R_{ro}}{R_j} \right)^3 \left(\frac{L_o}{L_i} \right) \left(\frac{C_i}{C_o} \right) \right]}, \tag{12}$$

where L_i and L_o are the inner length and the outer length of the floating ring, as shown in Fig. 3f.

Once the ring speed is known, the two Reynolds equations for the inner oil-film and the outer oil-film can be solved separately and the bearing dynamic coefficients can be obtained just like the conventional plain cylindrical bearing [35].

The nonlinear oil-film forces acting on the journal and the ring are determined as follows:

$$\begin{pmatrix} F_{ix} \\ F_{iy} \end{pmatrix} = \int_{-L_i/2}^{L_i/2} \int_0^{2\pi} p_i \begin{pmatrix} \cos \theta_i \\ \sin \theta_i \end{pmatrix} R_j \, d\theta_i \, dz_i, \tag{13}$$
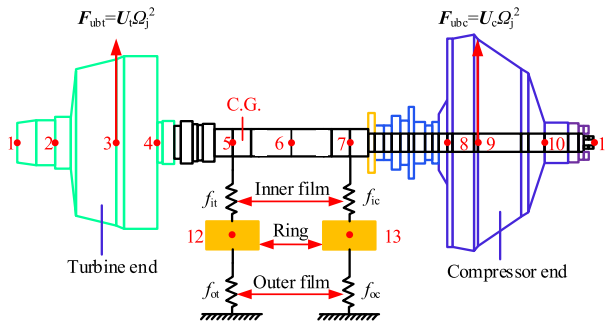
Fig. 5 FE model of a rotor-bearing system with 13 master nodes

Table 1 The impeller parameters

Part	Mass m (kg)	Polar inertia moment I_p (kg m^2)	Diameter inertia moment I_d (kg m^2)
TW	0.0607	5.88E−6	8.42E−6
CW	0.0212	2.76E−6	2.31E−6

$$\begin{pmatrix} F_{ox} \\ F_{oy} \end{pmatrix} = \int_{-L_o/2}^{L_o/2} \int_0^{2\pi} p_o \begin{pmatrix} \cos\theta_o \\ \sin\theta_o \end{pmatrix} R_{ro}\mathrm{d}\theta_o\mathrm{d}z_o. \tag{14}$$

At each time step of numerical integration, once the oil-film pressure distribution is solved, then the nonlinear oil-film forces are easy to be obtained by integrating the pressure distribution on the bearing surface domain. In this paper, the scalar pressure distribution is solved by using the FE method, and more details can refer to Ref. [36]. At the same instant, the Newmark-beta numerical integration algorithm is adopted to solve the response, where the two pressure distribution equations are linked into the system governing equations of motion introduced in the next section.

2.2 Motion equations of rotor-floating ring system

According to the rotor dynamics modeling principle and the assumptions mentioned earlier, an actual turbocharger rotor shown in Fig. 1 is discretized by using a series of master beam elements with internal beam sub-elements based on the FE method and Guyan reduction, as shown in Fig. 5. The moment of inertia, shear deformation and gyroscopic effect of each shaft element are considered. Each node of the beam element has four degrees of freedom (DOFs), i.e., two translational displacements and two rotational displacements. The floating ring is regarded as a pedestal (support).

The turbocharger rotor-floating ring system model is represented by a total of 10 master elements that include 41 sub-elements, along with two support elements used for two floating rings (see Fig. 5). The established FE model has a total of 12 nodes, where nodes 5 and 7 are the connection points used for the journal and the floating ring. Nodes 12 and 13 are for two floating rings due to its ring inertia. Nodes 3 and 9 are the C.G. positions of the turbine- and compressor-end impellers, respectively. The associated mass and rotational inertia for the impellers are listed in Table 1. Note that the C.G. of the turbocharger rotor system is very close to the turbine end bearing. This causes the load of the turbine end bearing to be more than ten times that of the compressor one.

The mass or stiffness (8×8) matrix of the beam element can be written in a general form:

$$A^{e} = \begin{bmatrix} a_{11} & & & & & & & \\ 0 & a_{22} & & & & \text{sym} & & \\ 0 & a_{32} & a_{33} & & & & & \\ a_{41} & 0 & 0 & a_{44} & & & & \\ a_{51} & 0 & 0 & a_{54} & a_{55} & & & \\ 0 & a_{62} & a_{63} & 0 & 0 & a_{66} & & \\ 0 & a_{72} & a_{73} & 0 & 0 & a_{76} & a_{77} & \\ a_{81} & 0 & 0 & a_{84} & a_{85} & 0 & 0 & a_{88} \end{bmatrix}, \tag{15}$$

where $a_{22} = a_{11}$, $a_{33} = a_{44}$, $a_{66} = a_{55}$, $a_{77} = a_{88}$, $a_{32} = -a_{41}$, $a_{62} = a_{51}$, $a_{72} = -a_{81}$, $a_{63} = -a_{54}$, $a_{73} = a_{84}$ and $a_{76} = -a_{85}$. The (4×4) beam element stiffness and translational/rotatory mass matrix in the *XZ* plane is a general form, which can be referred to any books or references about rotor dynamics, such as [37, 38].

Due to the existence of polar inertial moments, the gyroscopic matrix of the beam element is

$$G^{e} = \begin{bmatrix} 0 & & & & & & & \\ g_{21} & 0 & & & & \text{skew sym} & & \\ g_{31} & 0 & 0 & & & & & \\ 0 & g_{42} & g_{43} & 0 & & & & \\ 0 & g_{52} & g_{53} & 0 & 0 & & & \\ g_{61} & 0 & 0 & g_{64} & g_{65} & 0 & & \\ g_{71} & 0 & 0 & g_{74} & g_{75} & 0 & 0 & \\ 0 & g_{82} & g_{83} & 0 & 0 & g_{86} & g_{87} & 0 \end{bmatrix}, \tag{16}$$

where

$$g_{21} = \frac{-\rho I}{15L(1+\Phi)^2}(36), \quad g_{31} = \frac{\rho I}{15L(1+\Phi)^2}(3-15\Phi)L,$$

$$g_{43} = \frac{-\rho I}{15L(1+\Phi)^2}(4+5\Phi+10\Phi^2)L^2,$$

$$g_{83} = \frac{-\rho I}{15L(1+\Phi)^2}(-1-5\Phi+5\Phi^2)L^2,$$

$$g_{61} = -g_{21}, \; g_{71} = g_{31}, \; g_{42} = g_{31}, \; g_{52} = g_{21}, \; g_{82} = g_{31},$$

$$g_{53} = g_{31}, \; g_{64} = g_{31}, \; g_{74} = -g_{83}, \; g_{65} = g_{21}, \; g_{75} = -g_{31},$$

$$g_{86} = -g_{31}, \; g_{87} = g_{43}.$$

where ρ is the mass density; parameter I denotes area moment of inertia; L is the element length; E represents the elastic modulus; G denotes the shear modulus; and $\Phi = 12EI/(\kappa AGL^2)$, $\kappa = 0.886$.

After all the sub-element matrices which contained in each master element, are deduced into an 8×8 matrix. The assembly procedure of (40×40) complete matrices of the rotor system, (M_r, K_r, G_r), is depicted in Fig. 6.

Following the assembly process shown in Fig. 6, the motion governing equations with 44 DOFs describing the movement of the rotor are derived as:

$$M_r \ddot{q}_r + (C_r + \Omega_j G_r)\dot{q}_r + K_r q_r = F_{ub} + F_i + F_{sr}, \tag{17}$$
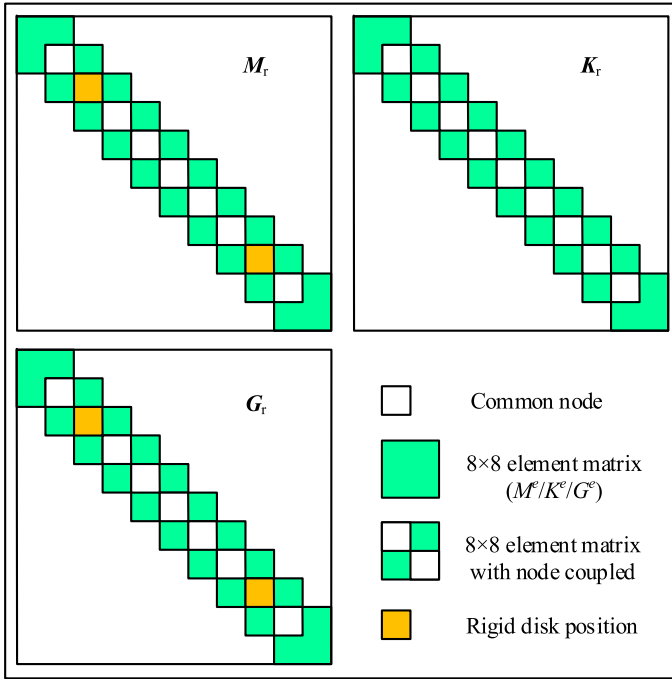
Fig. 6 Assembly schematic diagram of rotor total matrices

where $\boldsymbol{q}_r = [x_1, y_1, \psi_1, \varphi_1, \ldots, x_{11}, y_{11}, \psi_{11}, \varphi_{11}]^T$ is the displacement vector of the rotor. (x_n, y_n) and (ψ_n, φ_n) are the translational and the rotational displacements at the nth node, respectively. $\boldsymbol{M}_r$, $\boldsymbol{G}_r$ and $\boldsymbol{K}_r$ are the mass/inertia matrix, gyroscopic matrix and stiffness matrix, respectively. $\boldsymbol{F}_i$ is the inner oil-film force vector. $\boldsymbol{F}_{sr}$ represents the static force vector. Damping matrix, $\boldsymbol{C}_r$, is the Rayleigh damping form:

$$\boldsymbol{C}_r = \alpha \boldsymbol{M}_r + \beta \boldsymbol{K}_r, \tag{18}$$

where the formula for solving coefficients α and β can be referred to Refs. [39, 40].

$\boldsymbol{F}_{ub}$ is the unbalance force vector, which exists on the turbine and compressor impellers, corresponding to Nodes 3 and 9. Accordingly, the unbalance force can be written in a general form

$$\boldsymbol{F}_u = \begin{pmatrix} F_{ux} \\ F_{uy} \end{pmatrix} = \begin{pmatrix} me\dot{\phi}^2 \cos(\phi + \delta) + me\ddot{\phi} \sin(\phi + \delta) \\ me\dot{\phi}^2 \sin(\phi + \delta) - me\ddot{\phi} \cos(\phi + \delta) \end{pmatrix}, \tag{19}$$

where F_{ux} and F_{uy} are x and y components of unbalance force, respectively. ϕ denotes the rotation angle, and δ is the initial phase. m is unbalance mass, and parameter e represents the mass eccentricity. Under constant speed conditions, Eq. (19) is simplified as

$$\boldsymbol{F}_u = \begin{pmatrix} F_{ux} \\ F_{uy} \end{pmatrix} = \begin{pmatrix} me\Omega_j^2 \cos(\Omega_j t + \delta) \\ me\Omega_j^2 \sin(\Omega_j t + \delta) \end{pmatrix}, \tag{20}$$

Considering the coupling effect of floating rings and the rotor, the global motion equation of the turbocharger rotor-floating ring system is developed as follows:

$$
\begin{bmatrix} M_r & & \\ & M_{frt} & \\ & & M_{frc} \end{bmatrix} \begin{bmatrix} \ddot{q}_r \\ \ddot{q}_{frt} \\ \ddot{q}_{frc} \end{bmatrix} + \begin{bmatrix} C_r + \Omega_j G_r & & \\ & 0 & \\ & & 0 \end{bmatrix} \begin{bmatrix} \dot{q}_r \\ \dot{q}_{frt} \\ \dot{q}_{frc} \end{bmatrix}
$$
$$
+ \begin{bmatrix} K_r & & \\ & 0 & \\ & & 0 \end{bmatrix} \begin{bmatrix} q_r \\ q_{frt} \\ q_{frc} \end{bmatrix} = \begin{bmatrix} F_{ub} \\ 0 \\ 0 \end{bmatrix} + \begin{bmatrix} F_i \\ F_{iot} \\ F_{ioc} \end{bmatrix} + \begin{bmatrix} F_{sr} \\ F_{sfrt} \\ F_{sfrc} \end{bmatrix}, \tag{21}
$$

where $(M_{\text{frt}}, M_{\text{frc}})$, $(F_{\text{sfrt}}, F_{\text{sfrc}})$ and $(q_{\text{frt}}, q_{\text{frc}})$ are the mass/inertial matrices, gravity matrices and displacement vector for the turbine end and compressor end floating rings, respectively. The detailed motion governing equation of the ring was well documented in Refs. [3, 29, 30].

3 Linear analysis and model validation

Although the turbocharger is nonlinear in nature, linear predicted critical speeds and mode shapes are helpful to provide insight into the dynamic behaviors of the double overhung type rotor in which the turbine impeller is heavier than the compressor impeller, as mentioned in Sect. 2.2. What's more, the validation of modeling method should be done before carrying out the study of nonlinear dynamic characteristics. Meaningfully, causes of failure are also revealed. Firstly, the analysis of the critical speed and potential distribution are done. This section explains in part, from the perspective of mode shape and strain energy distribution, the failure is due to the enlargement in compressor end bearing inner clearance. Secondly, in order to validate the accuracy of the established turbocharger rotor model simulated by 11 master nodes and that of the validation of modeling method, the same rotor system shown in Fig. 1 is simulated 20 master nodes (see Fig. 7), then, the consistency between the results from these two simulation models is analyzed. Besides, the nonlinear response result is also compared with Ref. [1]. Finally, the simulation result about the resonance peak is compared with that of the test data recorded from balancing machine in the factory, which shows that operation wear will occur in the compressor end bearing. In simulations, material properties are listed in Table 2, and bearing parameter is summarized in Table 3.
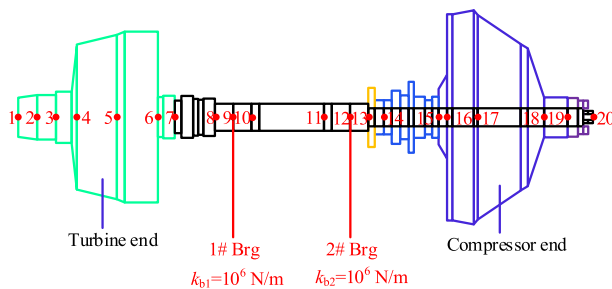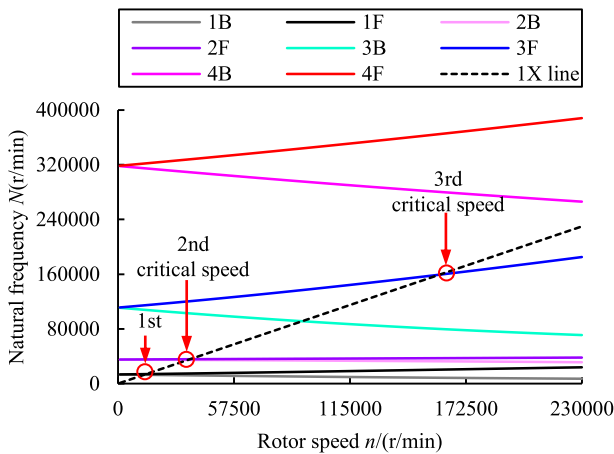

Fig. 7 Rotor model simulated by 20 master nodes

Table 2 Material details

No	Density $\rho/(kg/m^3)$	Elastic modulus $E/(GPa)$	Shear modulus $G/(GPa)$	Component
1	7850	205	80	Shaft
2	8100	105	40	Floating ring
3	7800	200	75	Nut

Table 3 Bearing details

| Parameter	Value	Parameter	Value
Ring mass/m_r	2.16 g	Left load/W_{t0}	0.932 N
Inner length/L_i	3.6 mm	Right load/W_{c0}	0.095 N
Outer length/L_o	6.15 mm	Oil number	10 W-30
Inner diameter/D_i	6.016 mm	Inner temp./T_i	102
Outer diameter/D_o	9.54 mm	Outer temp./T_o	95
Inner clearance/C_i	0.008 mm	Outer Clearance/C_o	0.03 mm

Fig. 8 Campbell diagram (bearing stiffness of 10^6 N/m)
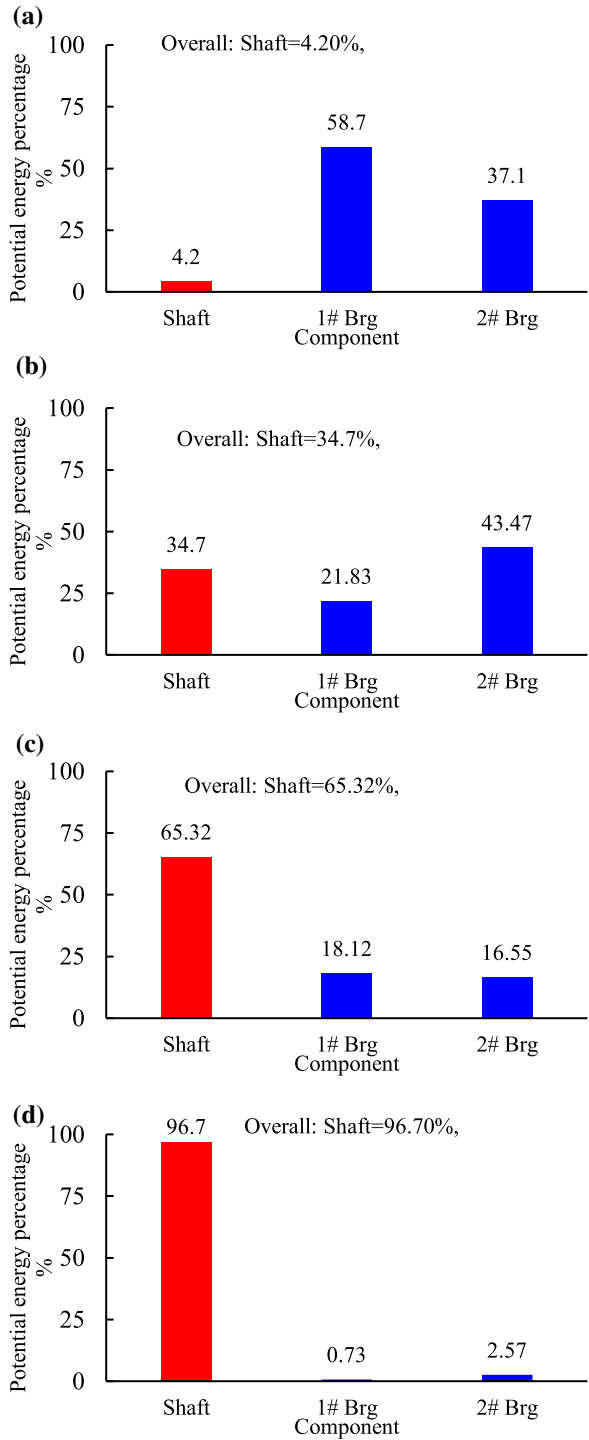
3.1 Critical speeds and energy distribution

Figure 8 shows the Campbell diagram of the established rotor model of 11 master nodes. It is assumed that the two supported bearings are simulated by linear springs with same constant stiffness of 10^3 N/mm [3]. The first 8 natural frequencies are numbered as 1B, 1F, 2B, 2F, 3B, 3F, 4B, 4F, where the B denotes the backward whirl and F denotes forward one. It can be seen that the first three critical speeds are 13,974 r/min, 35,716 r/min and 15,9131 r/min, respectively. Besides, the gyroscopic effect has a minimum influence on the second mode since the motion is predominated by the translational motion. The mode shapes and associated potential energy distribution for the first four critical speeds are shown in Figs. 9 and 10. The obtained mode shape results are in accordance with those shown in Refs. [3, 28, 30].

Fig. 9 Mode shapes: **a** the first
mode shape, **b** the second mode
shape, **c** the third mode shape and
d the fourth mode shape

(a)

(b)

(c)

(d)
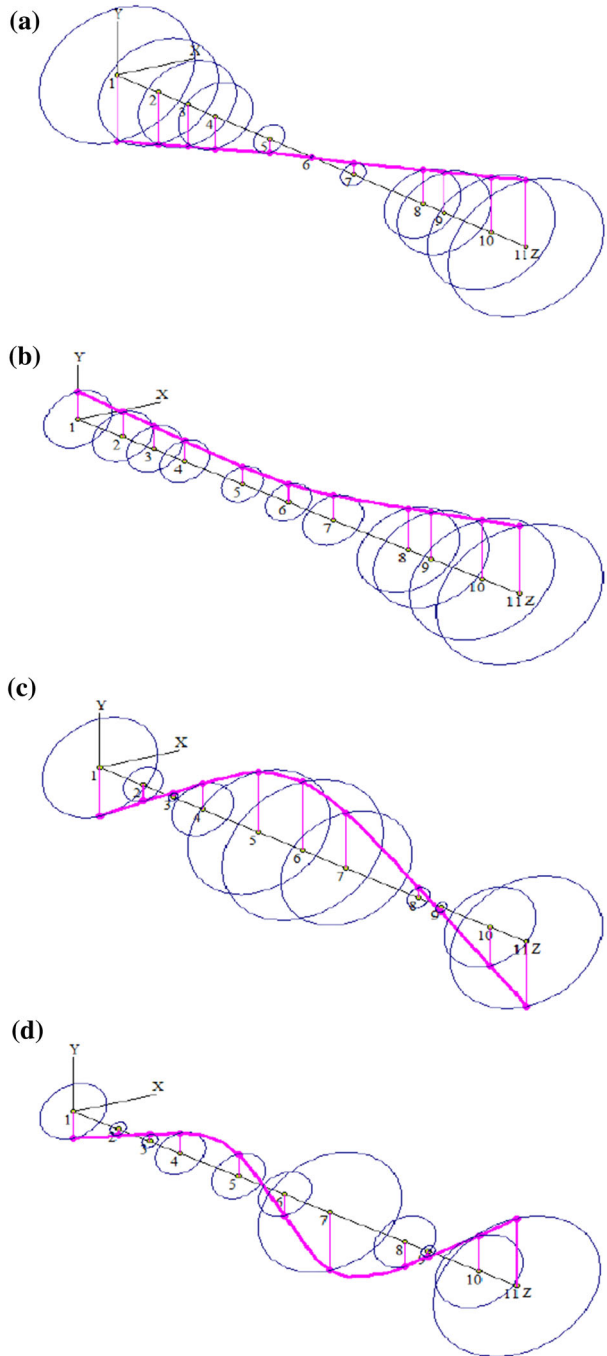
It shows that the first-order critical speed mode is a rigid body conical mode (see Fig. 9a)
as the turbocharger is designed to be a classic double overhung structure. Almost all the
potential energy is in two bearings, as shown in Fig. 10a. The second-order critical speed
mode shape shown in Fig. 9b is cylindrical, typically, the turbine and compressor impellers

Fig. 10 Strain energy distribution: **a** the first critical speed, **b** the second critical speed, **c** the third critical speed and **d** the fourth

Table 4 Critical speeds of two rotor models r/min

Critical speed	1	2	3	4
Model 1	13,974	35,716	159,166	485,229
Model 2	13,974	35,716	159,131	482,904

are in phase. Corresponding potential energy distribution shown in Fig. 10b shows that the maximum potential energy has been shifted to the compressor end bearing (2# brg) when the turbocharger rotor operates near at the second-order critical speed. Obviously, there is a considerable amount of bend at the shaft center. As shown in Fig. 5, the C.G. of rotor system is very close to the turbine side bearing (1# brg). Therefore, in the second whirling mode, the motion amplitude of the turbine side is moderate and a greater amplitude of motion is observed at the compressor one, as shown in Fig. 9b. This indicates that the compressor end bearing will wear out over time and finally causes failure, which is in accordance with the fact that in all failed practical turbochargers, more wear appears in the compressor end bearing.

Figure 9c, d shows the third-order and fourth-order critical speed mode are the first bending mode and the second bending mode, in which most of the potential energy in the shaft, i.e., 65.32% for the third critical speed mode and 96.7% for the fourth critical speed mode. In general, the operating speed is lower than the bending critical speeds, since the bearings have little damping effect to the strain energy on the bending rotor.

3.2 Model validation: 10 nodes versus 20 nodes

In order to validate the accuracy of the rotor system model using 10 master elements with 11 master nodes, the same system is modeled by increasing the master nodes to 20, as mentioned above and shown in Fig. 7. The two supported bearings are also modeled by linear springs with the same constant stiffness of 10^3 N/mm. A comparison of the first four-order critical speeds for these two different models is shown in Table 4. The result shows that there is a small difference for the 1rd and 4th critical speeds of these two refined rotor models, which well validate the accuracy of the 11-master-nodes rotor model.

3.3 Model validation: comparison with Ref. [1]

In order to validate the reasonability of the nonlinear response of the dynamic model established by using the proposed modeling method in this paper, the response is solved using the Newmark-beta algorithm and compared with the published literature result. As shown in Fig. 11, the spectrum bifurcation sequence has good consistency, which shows the effectiveness of the proposed modeling method in this paper to some extent.

3.4 Model validation: simulation versus test data

The steady-state synchronous response simulation result at speed range from 10,000 to 230,000 r/min is shown in Fig. 12a. The balancing machine is shown in Fig. 12b, and the test result is shown in Fig. 12c. It can be seen that amplitude peaks of the simulation and test are, respectively, appears at 59,000 r/min and 56,000 r/min. Accordingly, the difference between simulation results and experimental results is in acceptable range which further validates the effectiveness of the model established.

According to the data from Sect. 3.1, this critical speed is judged as the second mode in which the turbine impeller and compressor impeller are moving in phase, while the first
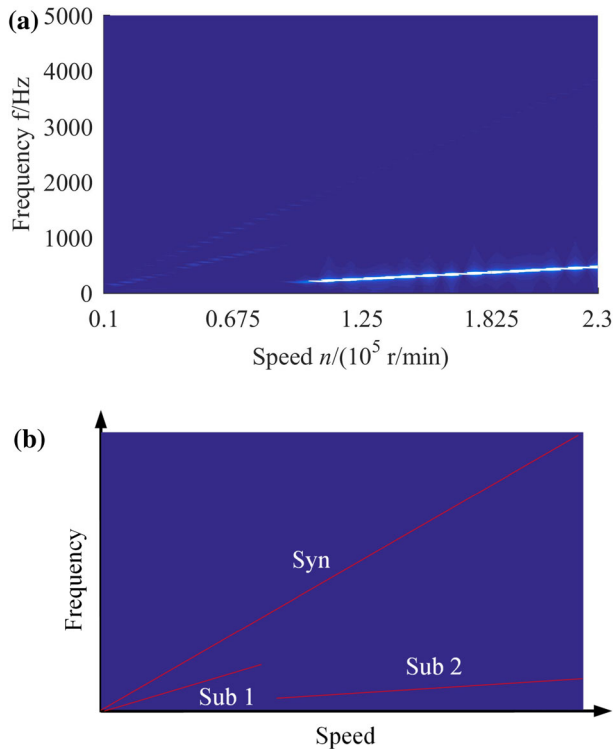
Fig. 11 Comparisons of frequency spectrum: **a** result in this paper, **b** result in Ref. [1]

critical speed is well damped. As analyzed earlier, when the rotor whirls in this mode, the vibration displacement of the compressor end bearing is larger than that of the turbine one. Unlike diesel engines used in trucks, car turbochargers run over a wide speed range [41–43]. The turbocharger speed-up or speed-down through the speed range from 55,000 to 60,000 r/min could cause additional wear and degradation to the compressor end bearing. These in-depth indicate that the compressor end bearing wears out over time. Namely, the inner clearance at compressor end bearings will open up gradually.

4 Numerical simulation and discussion

According to the results shown in Sect. 3 and the practical observation, it is concluded that the compressor end bearing inner clearance will be increased over time during the operation. Thus, the bearing clearance and unbalance are taken as control parameters. In this section, in order to predict the dynamic behavior with the variation of compressor end bearing inner clearance, the nonlinear numerical simulation results of a perfectly balanced rotor (mass unbalance offset $e = 0$ for both impellers) will first be presented in Sect. 4.1. The coupling of the mass unbalance is introduced in Sect. 4.2 to show the rotor dynamic evolution characteristics with the increase of compressor end bearing inner clearance in real practices, since turbochargers as well as other rotational machines are difficult to be perfectly balanced. Finally, a comparative analysis of the perfectly balanced rotor and the inherently

(a)

(b)

(c)
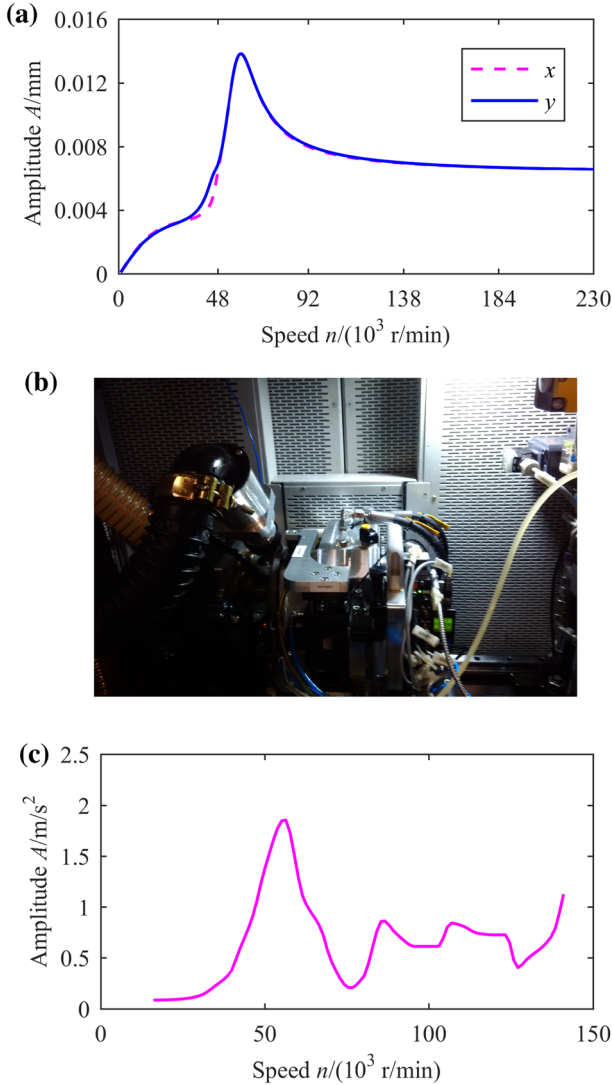
Fig. 12 Response Comparisons: **a** simulation result, **b** balancing machine and **c** test result

unbalanced rotor is done in Sect. 4.3 to illustrate the applicability of the results obtained under ideal conditions shown in Sect. 4.1.

According to the actual possible wear condition [9] of the two supported floating ring bearings for all failed turbochargers observed and the turbocharger failure reasons described in Sect. 3, it come to a conclusion that the compressor end bearing inner clearance will increase significantly with the wear of the floating ring inner surface over time, which will eventually lead to the failure of the turbocharger, due to the special structure design with the feature of double overhung rotor, the position of the mass center of the total system very closer to the turbine end bearing and the same design for the two supported bearings.

Table 5 Enlargement of bearing inner clearance

Inner clearance at CWE	$1c_i$	$2c_i$	$3c_i$	$4c_i$	$5c_i$
Value (mm)	0.008	0.016	0.024	0.032	0.040

According to the statistical data from the turbocharger manufacturer, for investigation purpose, it is assumed that compressor end bearing inner clearance increases from the initial value ($1c_i \approx 0.5$ mil) to 5 times ($5c_i \approx 2.5$ mils) the initial nominal value. Note that Ref. [39] showed one failed turbocharger (a shaft fracture accident occurred at the turbine end) compressor end bearing had the inner clearance enlarged to over five mils.

Table 5 shows the enlargement of inner clearance at the compressor impeller end (CWE) due to the wear of inner surface of the floating ring during operation.

4.1 Dynamics behaviors with the variation of inner clearance for a perfectly balanced rotor

According to the analysis in Sect. 3 mentioned above, there is no doubt that the compressor end bearing inner clearance will be gradually enlarged over time. In order to predict the dynamics behaviors under the enlargement of inner clearance at the compressor end bearing, the inner clearance and speed are both taken as control parameters.

The three-dimensional (3D) spectrums (waterfall plots) of Node 9 in the horizontal direction for the turbocharger rotors with different CWE bearing inner clearances and the corresponding vibration single peak value (SPV) are shown in Fig. 13. As can be seen from Fig. 13a–e, regardless of the variation of the inner clearance, the turbocharger rotor-bearing system becomes unstable at a very low rotational speed (at the starting of simulation). For this instability, the oil whirl/whip in the inner oil-films excites the gyroscopic conical forward mode with Sub 1 frequency component. Most noteworthy, under different bearing inner clearances, is that the variation trend of the frequency component that dominates the rotor motion with speed is basically the same, except the onset speed of Sub 2 instability, which excites the conical forward mode caused by the outer oil-films. That is to say, the parameter of inner clearance has a significant effect on the Sub 2 instability threshold: the onset speeds of Sub 2 instability under $1c_i$, $2c_i$, $3c_i$, $4c_i$, $5c_i$ are, respectively, 100,000 r/min, 115,000 r/min, 105,000r/min, 90,000 r/min, the start speed of simulation; With the increase in bearing inner clearance from 1 to $2c_i$, the increment of the onset speed of Sub 2 instability is around 15,000 r/min, which reduced by 15%; However, the instability threshold decreases with the further increase in bearing inner clearance; What's more surprising is that when the rotor is running with $5c_i$, the instability caused by Sub 2 mode starts at the beginning of simulation (see Fig. 13e); If the rotor system operates under this condition, it will fail quickly, such as the blade degradation of the compressor impeller and the shaft fracture caused by the violent rub contact between the compressor impeller and the volute. Therefore, as the compressor end bearing inner clearance increases to a certain level, the stability of the turbocharger rotor-bearing system will be significantly deteriorated.

The SPV-speed curves depicted in Fig. 13f show that the amplitudes of rotor motion, for different compressor end bearing inner clearances, decrease firstly and then increase with the rotational speed. As the inner clearance increases from 1 to $2c_i$, amplitudes are increased at most rotational speeds, except the speed range from 70,000 to 170,000 r/min. With the further increase in inner clearance to $3c_i$, the speed range for the reduction of motion amplitude compared to $1c_i$ is from 70,000 to 90,000 r/min, which is shrunk to a narrower region than that of $2c_i$. In comparison with $2c_i$, however, the amplitude of the rotor motion for $3c_i$ is increased over the speed range considered. As predicted, the inner surface of the
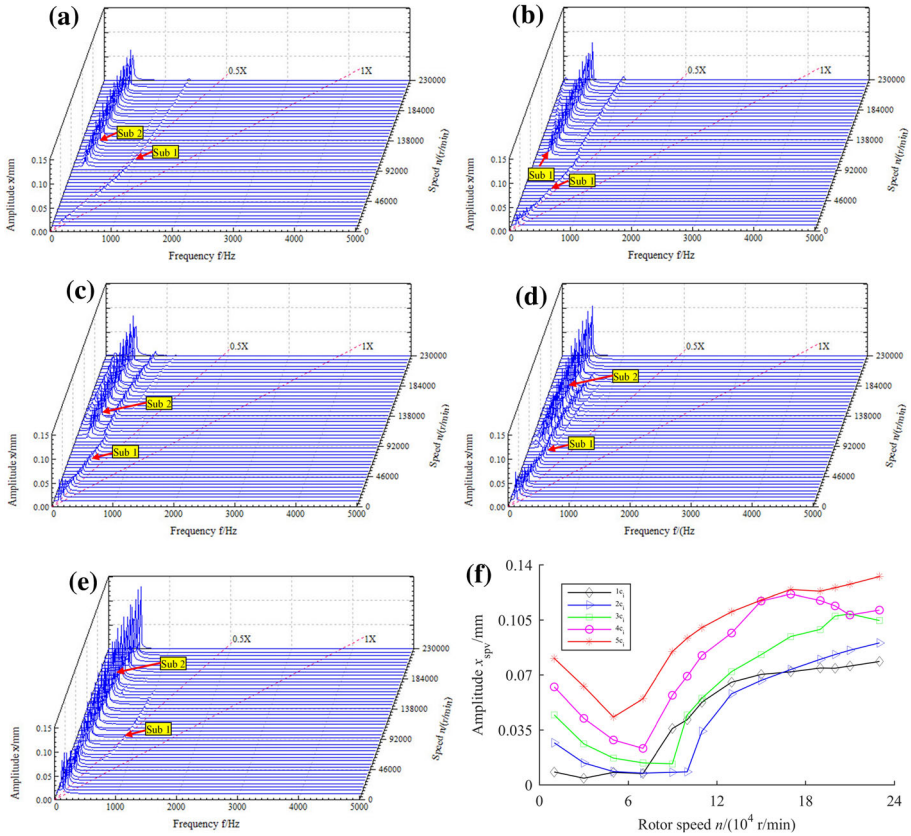
Fig. 13 Waterfall plots and SPV-speed curves: **a** $1c_i$ (initial design value), **b** $2c_i$, **c** $3c_i$, **d** $4c_i$, **e** $5c_i$ and **f** SPV-speed curves for different compressor end bearing inner clearances

compressor end floating ring continues to wear over time, resulting in an increase in inner clearance. When the inner clearance is further enlarged to $4c_i$ or $5c_i$, the total amplitude of the turbocharger rotor increases rapidly over the speed range. For all inner clearance conditions, there is no doubt that the rotor amplitude increases with the enlargement in compressor end bearing inner clearance when turbochargers operate at lower or higher speeds. Based upon the above analysis, it is concluded that in most of the operating speeds, the rotor amplitude continues to grow with the increase in the bearing inner clearance at compressor end.

In order to further reveal the compressor end bearing will wear over time and finally causes failure, and to reveal the evolutional process of the whirl orbits with the increase in the inner clearance, the 3D processional orbits of the rotor at four speeds under different inner clearances are obtained, as shown in Fig. 14. It can be found from Fig. 14a that when the inner clearance is in the $1c_i$, the sub-synchronous whirl mode of 50,000 r/min is a cylindrical mode similar to the 2nd critical speed mode in which the compressor and turbine are in phase. In this mode, the motion amplitude of compressor is larger than that of the turbine. However, at other rotational speeds ($n = 100,000$ r/min, 150,000 r/min and 200,000 r/min), the sub-synchronous modes are all conical rigid modes in which the motion amplitude of the turbine end bearing larger than that of the compressor one. As the turbocharger repeatedly
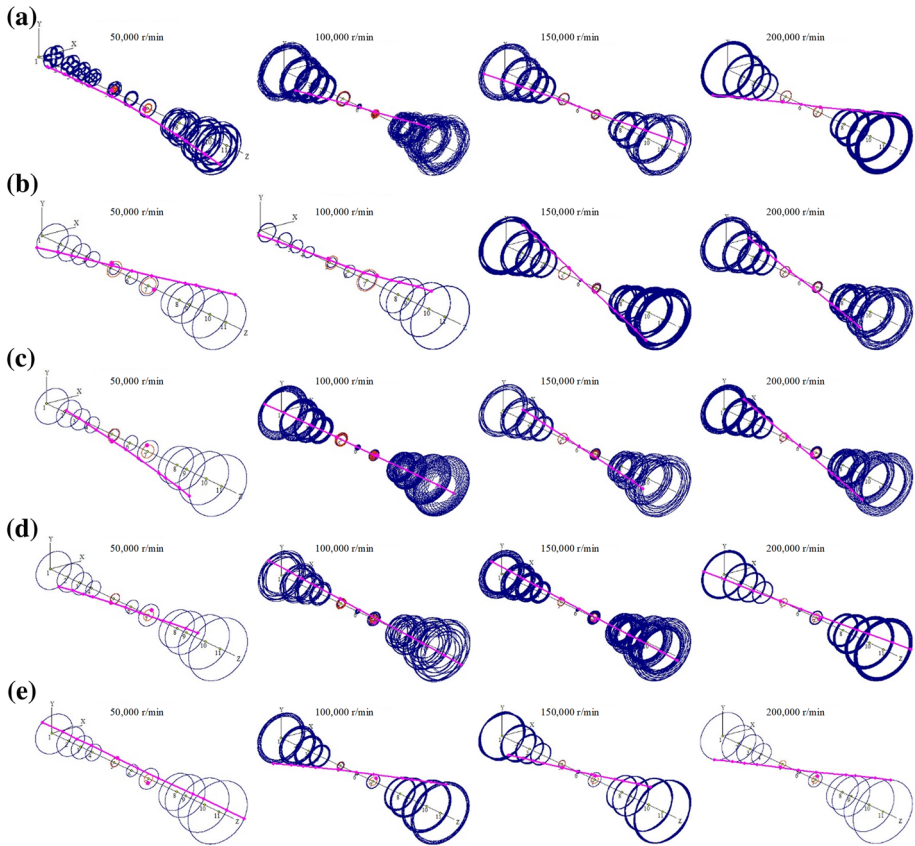
Fig. 14 Rotor 3D processional orbits: **a** $1c_i$ (initial design value), **b** $2c_i$, **c** $3c_i$, **d** $4c_i$ and **e** $5c_i$

run-up and run-down through the second mode critical speed, in the actual complex running process of cars, the higher motion amplitude at the compressor bearing will wear away the inner surface of its ring. Therefore, as time goes by, the inner clearance at compressor end bearing will be gradually enlarged. When the inner clearance increases to $2c_i$, the instability mode at 50,000 r/min is transformed into the conical whirl mode compared to the cylindrical whirl mode for $1c_i$. Obviously, the motion amplitude of the compressor end bearing begins to be larger than that of the turbine end bearing at 50,000 r/min and 100,000 r/min. However, there is little change in the sub-synchronous whirl modes at 150,000 r/min and 200,000 r/min. With the further increase of inner clearance, as shown in Fig. 14c–e, the motion amplitude of the compressor end bearing is larger than that of the turbine end bearing at each speed.

Since the predominant unstable motion mode is the first critical conical rigid mode, as shown in Fig. 14a–e, small increases in the inner clearance will cause the motion amplitude of the compressor end bearing to be gradually larger than that of the turbine end bearing and allow compressor impeller to contact the volute causing blade damage. And these finally cause failure to turbochargers.

4.2 Dynamics behaviors with the variation of inner clearance for a rotor with inherent mass unbalance

Since turbochargers as well as other rotational machines are impossible to be perfectly balanced (zero unbalance) in the real practices, the objective of this subsection is to demonstrate the applicability of the results obtained in Sect. 4.1 by applying the unbalance on the established turbocharger rotor-bearing system model. The same level of unbalance (*me* = 0.1 g mm) is applied to the center of mass of two impellers. This level of mass unbalance is typical of this class of turbochargers. It should be pointed out that only in-phase unbalance is considered, which means $\delta_t = \delta_c = 0$ (see Eq. 19, Subscripts t and c are used to distinguish turbine and compressor side parameters).

The waterfall plots of Node 9 in the horizontal direction for the turbocharger rotor with unbalance defect operating with different compressor end bearing inner clearances and the corresponding vibration SPV are shown in Fig. 15. The results show that the imposed unbalance can hardly affect the vibration characteristics as compared to the results given in Fig. 13. Namely, with the increase in compressor end bearing inner clearance, the changing tendencies of the sub-synchronous frequency component, the total vibration amplitude and the stability of the rotor are basically in accordance with the results obtained in Sect. 4.1. One reason for this is that the inner clearance at the compressor end has a great influence on the rotor vibration in these two working conditions.

As a result, with a given compressor end bearing inner clearance value, the simulation result with the perfectly balanced rotor can well capture the principal vibration characteristics of the turbocharger. So, the enlargement of the compressor end bearing inner clearance will lead to degradation in system stability, increment in vibration level, and ultimately lead to failure of the turbocharger.
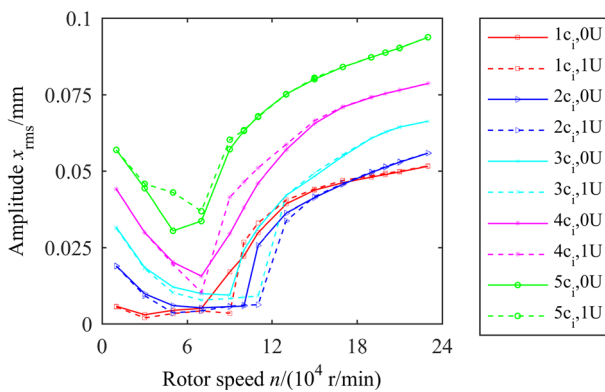
4.3 Comparative analysis and discussion

Figure 16 represents the vibration root-mean-square (RMS) value of Node 9 in the horizontal direction for the perfectly balanced and inherently unbalanced turbocharger rotors with different compressor end bearing inner clearances, when the speed range considered from 10,000 to 230,000 r/min. With different inner clearances at compressor end bearing, it is apparent that the difference of the vibration RMS value between these two rotors with or without inherent mass unbalance is not enough to disturb the inner clearance effect on the vibration response. Most notably, the inner clearance has the ability to increase the amplitude of system response considerably at the entire rotor speed range considered, provided that the inner clearance is enlarged enough. Although bearing wear at the compressor end is inevitable, in order to ensure the safe operation of the rotor and avoid failure in advance, the inner clearance should be guaranteed within 3 ci, preferably within 2 ci, otherwise, the floating ring bearing at the compressor end must be replaced in time.

In order for the turbocharger to be able to run with stable limit cycle orbits, the inner bearing clearances must be kept very small. In addition, as the turbocharger repeatedly run-up and run-down through the second critical speed mode, in which the turbine end maintains a fairly small amplitude while large motion amplitude is in the compressor end (see Fig. 14a), the higher motion amplitude at the compressor end bearing will wear away the inner surface of its ring. Since the predominate turbocharger whirl mode (see Fig. 14) is a conical rigid mode similar to the first critical speed mode shown in Fig. 9a, any increase in the compressor end bearing inner clearance continues to increase the sub-synchronous conical whirl amplitude of motion and will allow the compressor impeller to contact the volute. This causes either
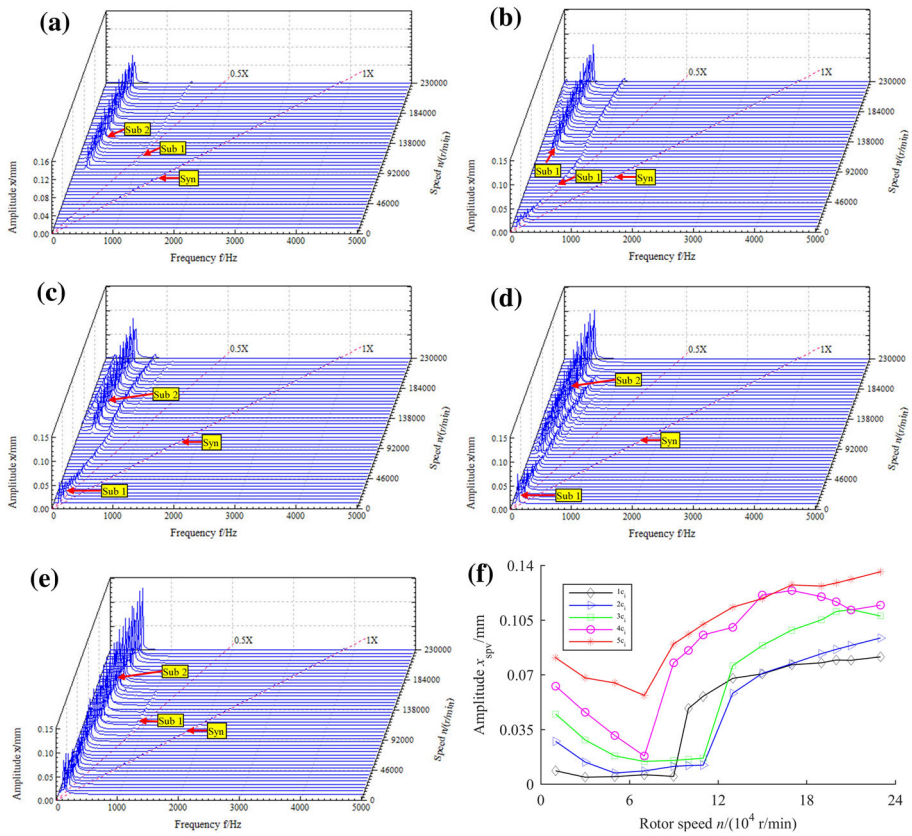
Fig. 15 Waterfall plots and SPV-speed curves when 0.1 g mm unbalance applied on the two impellers: **a** $1c_i$, **b** $2c_i$, **c** $3c_i$, **d** $4c_i$, **e** $5c_i$ and **f** SPV-speed curves

Fig. 16 Vibration root-mean-square value-speed curves

damage to the compressor blades, or to fatal turbine shaft fracture failure due to hard rub between the impeller and the volute.

From the above analysis and discussion, it can be seen that the dynamic evolution characteristics of turbochargers with the increase in inner clearance at the compressor end bearing is well revealed, and the main reason for rotor failure is obtained. Additionally, it explains well why more damage is often observed on compressor end bearings in practices. Critically, the study also proposes a general refined turbocharger rotor modeling method to predict the dynamics behaviors efficiently.

5 Conclusion

In this paper, the prediction of dynamic behaviors and failure of an actual turbocharger rotor supported by floating ring bearing are investigated. This work presents an efficient and general refined flexible rotor model considering the variable cross-section rotor feature based on the FE method and Guyan reduction. By coupling the ring motion equation with the governing equation of the turbocharger rotor, a thirteen master-nodes coupling 41 sub-nodes rotor-floating ring multi-body dynamic model is established. The accuracy and efficiency of the proposed rotor modeling method are verified by comparing it with the same rotor simulated by more nodes, similar result from the published literature and the test data recorded. According to the vibration feature of turbocharger rotors, furthermore, the influence of the bearing inner clearance at compressor end on vibration characteristics, while the rotor with and without unbalance defect, is also discussed. The main conclusions are drawn as follows:

(1) The accuracy of the proposed rotor modeling method that fully considers the rotor flexibility and the variable cross-section feature is in agree well with the test result. The calculation efficiency is higher than the common FE method due to fewer DOFs after conducting condensation.

(2) The major failure mode of turbochargers is revealed. The inner clearance at compressor end continues to enlarge over time. As the predominate turbocharger whirl mode is a conical rigid mode similar to the first-order critical speed mode, any enlargement in the compressor end bearing inner clearance continues to increase the sub-synchronous conical whirl amplitude, which will allow the compressor impeller to touch the volute. This causes finally either the damage to compressor blades, or to fatal turbine shaft fracture due to the hard rub between the impeller and volute.

(3) The dynamics behaviors of the turbocharger during operation are well obtained. The variation of compressor end bearing inner clearance will causes significant changes not only on the stability bus also the total vibration level as well as the whirl mode, due to the change of dynamic characteristic coefficient. In order to ensure safe operation and avoid sudden shaft fracture failure, the compressor end bearing inner clearance should be guaranteed within $3c_i$, preferably within $2c_i$, otherwise, the bearing at compressor end must be replaced in time.

The above research is helpful to further predict the dynamic behavior and faults of the turbocharger. Although the proposed rotor modeling method is applied to study the turbocharger, it can be applied on other complex rotor system, such as aero-engines. Future research will focus on the redesign of the compressor end bearing and the rearrangement of the center of gravity position of the rotor system for improved lubrication and stability. In addition, a detailed vibration test about bearing redesign will also be performed.

Presciently, this problem will eventually be resolved by the rapid switch to the electric vehicles.

Declarations

Conflict of interest The authors declare that they have no known competing financial interests or personal relationships that could have appeared to influence the work reported in this paper.

References

1. B. Schweizer, Dynamics and stability of turbocharger rotors. Arch. Appl. Mech. **80**(9), 1017–1043 (2010)
2. A. Singh, T.C. Gupta, Effect of rotating unbalance and engine excitations on the nonlinear dynamic response of turbocharger flexible rotor system supported on floating ring bearings. Arch. Appl. Mech. **90**, 1117–1134 (2020)
3. L. Tian, W.J. Wang, Z.J. Peng, Effects of bearing outer clearance on the dynamic behaviours of the full floating ring bearing supported turbocharger rotor. Mech. Syst. Signal Process **31**, 155–175 (2012)
4. B. Schweizer, M. Sievert, Nonlinear oscillations of automotive turbocharger turbines. J. Sound Vib. **321**, 955–975 (2009)
5. B. Schweizer, Oil Whirl, oil whip and whirl/whip synchronization occurring in rotor systems with full-floating ring bearings. Nonlinear Dyn. **57**, 509–532 (2009)
6. B. Schweizer, Vibrations and bifurcations of turbocharger rotors. In: SIRM 2009—8th International Conference on Vibrations in Rotating Machines, Paper-ID 23, Vienna, Austria, 23–25 February (2009), ISBN 978–3–200–01412–1.
7. B. Schweizer, Total instability of turbocharger rotors—physical explanation of the dynamic failure of rotors with full-floating ring bearings. J. Sound Vib. **328**(1–2), 156–190 (2009)
8. L.S. Andres, J.C. Rivadeneira, K. Gjika, C. Groves, G. Larue, Rotordynamics of small turbochargers supported on floating ring bearings-highlights in bearing analysis and experimental validation. J. Tribol. **129**(2), 391–397 (2007)
9. E.J. Gunter. Failure analysis of 2 liter engine turbochargers, https://www.researchgate.net/publication/342515831_FAILURE_ANALYSIS_OF_2_LITER_ENGINE_TURBOCHARGERS;2020. Accessed 26 March 2021.
10. P. Koutsovasilis, N. Driot, D. Lu, B. Schweizer, Quantification of sub-synchronous vibrations for turbocharger rotors with full-floating ring bearings. Arch. Appl. Mech. **85**, 481–502 (2015)
11. A. Andrearczyk, P. Bagiński, P. Klonowicz, Numerical and experimental investigations of a turbocharger with a compressor wheel made of additively manufactured plastic. Int. J. Mech. Sci. **178**, 105613 (2020)
12. P. Novotný, J. Hrabovský, J. Juračka, J. Klíma, V. Hort, Effective thrust bearing model for simulations of transient rotor dynamics. Int. J. Mech. Sci. **157–158**, 374–383 (2019)
13. P. Novotný, J. Hrabovský, Efficient computational modelling of low loaded bearings of turbocharger rotors. Int. J. Mech. Sci. **174**, 105505 (2020)
14. P. Novotný, P. Škara, J. Hliník, The effective computational model of the hydrodynamics journal floating ring bearing for simulations of long transient regimes of turbocharger rotor dynamics. Int. J. Mech. Sci. **148**, 611–619 (2018)
15. P. Novotný, M. Jonák, J. Vacula, Evolutionary optimisation of the thrust bearing considering multiple operating conditions in turbomachinery. Int. J. Mech. Sci. **195**, 106240 (2021)
16. E. Woschke, C. Daniel, S. Nitzschke, Excitation mechanisms of non-linear rotor systems with floating ring bearings-simulation and validation. Int. J. Mech. Sci. **134**, 15–27 (2017)
17. L. Smolík, Š Dyk, Towards efficient and vibration-reducing full-floating ring bearings in turbochargers. Int. J. Mech. Sci. **175**, 105516 (2020)

18. R.G. Kirk, A.A. Alsaeed, Induced unbalance as a method for improving the dynamic stability of high-speed turbochargers. Int. J. Rotat. Mach **952869**, 1–9 (2011)
19. R.G. Kirk, A.A. Kornhauser, J. Sterling, A. Alsaeed, Turbocharger on-engine experimental vibration testing. J. Vib. Control **16**(3), 343–355 (2010)
20. R.G. Kirk. Experimental evaluation of hydrodynamic bearings for a high speed turbocharger. J. Eng. Gas. Turb. Power 2014; 136: 072501-1-072501-9.
21. Š. Dyk, L. Smolík, M. Hajžman, Effect of various analytical descriptions of hydrodynamic forces on dynamics of turbochargers supported by floating ring bearings. Tribol. Int. **126**, 65–79 (2018)
22. G.C. Ying, G. Meng, J.P. Jing, Turbocharger rotor dynamics with foundation excitation. Arch. Appl. Mech. **79**(4), 287–299 (2009)
23. C.H. Li, Dynamics of rotor bearing systems supported by floating ring bearings. J. Lubr. Technol. **104**(4), 469–477 (1982)
24. L. Feng, M. Zhou, Q.Y. Xu, Effects of semi-floating ring bearing outer clearances on the subsynchronous oscillation of turbocharger rotor. Chin. J. Mech. Eng-Eng. **29**(5), 901–909 (2016)
25. L.K. Wang, G.F. Bin, X.J. Li, X.F. Zhang, Effects of floating ring bearing manufacturing tolerance clearances on the dynamic characteristics for turbocharger. Chin. J. Mech. Eng-Eng. **28**(3), 530–539 (2015)
26. L.K. Wang, G.F. Bin, X.J. Li, D.Q. Liu, Effects of unbalance location on dynamic characteristics of high-speed gasoline engine turbocharger with floating ring bearings. Chin. J. Mech. Eng-Eng. **29**(2), 271–280 (2016)
27. G.F. Bin, Y. Huang, X.L. Zhong, F. Yang, Z.Y. Mao, Effect of inlet oil temperature on vibration characteristics of high-speed light-load turbocharger rotor under long period and variable speed. J. Mech. Eng. **56**(21), 131–139 (2020)
28. G.F. Bin, Y. Huang, X.L. Zhong, F. Yang, Study on the influence of floating ring axial length on vibration characteristics of high-speed and light-load turbocharger rotor system. J. Mech. Eng. **55**(23), 174–180 (2019)
29. L. Tian, W.J. Wang, Z.J. Peng, Nonlinear effects of unbalance in the rotor-floating ring bearing system of turbochargers. Mech. Syst. Signal Process **34**(1–2), 298–320 (2013)
30. L. Smolík, M. Hajžman, M. Byrtus, Investigation of bearing clearance effects in dynamics of turbochargers. Int. J. Mech. Sci. **127**, 62–72 (2017)
31. H. Nguyen-Schäfer, *Nonlinear rotordynamics of turbochargers* (Springer, Berlin, 2012)
32. W.J. Chen, E.J. Gunter, *Introduction to Dynamics of Rotor-Bearing Systems* (Trafford Publishing, Victoria, 2010)
33. L.K. Wang, A.L. Wang, M. Jin, Y.J. Yin, Bistable vibration characteristics of rod fastening rotor with internal damping. China Mech. Eng. **32**(5), 512–522 (2021)
34. E.J. Gunter, W.J. Chen. Dynamic analysis of a turbocharger in floating bushing bearings. In: Proceedings of the Third International Symposium on Stability Control of Rotating Machinery (ISCORMA), Cleveland, OH, USA, September 19–23, 2005.
35. R.G. Krik, A.A. Alsaeed, E.J. Gunter, Stability analysis of a high-speed automotive turbocharger. Tribol. Trans. **50**, 427–434 (2007)
36. W.J. Chen. Practical rotordynamics and fluid film bearing design. Eigen Technologies, Incorporated; 2015.
37. M. Friswell, *Dynamics of Rotating Machines* (Cambridge University Press, Cambridge, 2010)
38. L.K. Wang, A.L. Wang, M. Jin, Y.J. Yin, X. Heng, P.W. Ma, Nonlinear dynamic response and stability of a rod fastening rotor with internal damping effect. Arch. Appl. Mech. **91**, 3851–3867 (2021)
39. L.K. Wang, A.L. Wang, M. Jin, Q.K. Huang, Y.J. Yin, Nonlinear effects of induced unbalance in the rod fastening rotor-bearing system considering nonlinear contact. Arch. Appl. Mech. **90**, 917–943 (2020)
40. Y.Q. Li, Z. Luo, J.X. Liu, H. Ma, D.S. Yang, Dynamic modeling and stability analysis of a rotor-bearing system with bolted-disk joint. Mech. Syst. Signal Process **158**, 107778 (2021)
41. C. Zhang, Y. Wang, R. Men, H. He, W. Chen, Dynamic behaviors of a high-speed turbocharger rotor on elliptical floating-ring bearings. Proc. Inst. Mech. Eng. Part J. **233**(12), 1785–1799 (2019)
42. A. Grönman, P. Sallinen, J. Honkatukia, J. Backman, A. Uusitalo, Design and experiments of two-stage intercooled electrically assisted turbocharger. Energy Convers. Manag. **111**, 115–124 (2016)
43. W.J. Chen, Rotordynamics and bearing design of turbochargers. Mech. Syst. Signal Process **29**(7), 77–89 (2012)